Rotating vortices in two-dimensional inhomogeneous strongly coupled dusty plasmas: Shear and spiral density waves

Vikram S. Dharodi*

Department of Mechanical Engineering, Michigan State University, East Lansing, Michigan 48824, USA

(Received 17 July 2020; accepted 12 October 2020; published 28 October 2020)

Dusty plasma experiments can be performed quite easily in a strong coupling regime. In our previous work [V. S. Dharodi, S. K. Tiwari, and A. Das, Physics of Plasmas **21**, 073705 (2014)], we numerically explored such plasmas with constant density and observed the transverse shear (TS) waves from the rotating vortex. Laboratory dusty plasmas are good examples of homogeneous plasmas; however, heterogeneity (e.g., density, temperature, and charge) may be due to the existence of voids, different domains with different orientations, presence of external forces like magnetic and/or electric, size or charge imbalance, etc. Here, we examine how the density heterogeneity in dusty plasmas responds to the circularly rotating vortex monopoles, specifically, smooth and sharp cutoff. For this purpose, we have carried out a series of two-dimensional fluid simulations in the framework of the incompressible generalized hydrodynamics fluid model. The rotating vortices are placed at the interface of two incompressible fluids with different densities. The smooth rotating vortex causes two effects: First, the regions are stretched to form the spiral density waves; second, there is a shear in flows which consequently induces the TS waves. The TS waves move slower in the denser side than in the lighter side. The difference in speeds of the waves induces the net flow of the medium towards the lower density side. We notice that the spiral density arms are distinguishable in the early time while later they get smeared out. In sharp flows, the interplay between the TS waves and the vortices of Kelvin-Helmholtz instability distorts the formation of the regular spiral density arms around the rotor.

DOI: 10.1103/PhysRevE.102.043216

I. INTRODUCTION

A typical fluid or turbulent flow contains a wide variety of coherent structures [1] like rotating monopoles and tripoles [2,3] and propagating and merging dipoles [4]. It becomes important to understand how such types of structures encounter the density and/or temperature gradient in a medium, which may cause the formation of different kinds of waves like acoustic [5–7], shock [8–10], spiral [11,12], and transverse [13–18] and fluid instabilities like Kelvin-Helmholtz (KH) [19,20] and Rayleigh-Taylor [21,22]. Laboratory dusty plasmas are good examples of homogeneous plasmas; however, heterogeneity (e.g., density, temperature, and charge) may be due to the existence of voids, different domains with different orientations, presence of external forces like magnetic and/or electric, size or charge imbalance, etc. Our objective here is to understand how the density heterogeneity in a strongly coupled state responds to the coherent structures (here, rotating vortex monopoles). For this purpose we specifically here consider the case of two-dimensional (2D) dusty plasmas. The motivational factors that induce us to choose such 2D plasmas are the following: 2D dusty plasmas are favored in laboratory experiments [23–29] and simulations [10,30–33], dusty plasmas can exist in strong coupling states quite easily because of high charged dust particles, and in dusty plasmas a coherent structure can survive for a longer time than in a hydrodynamic fluid (viscosity shows pure damping effect) because the effect of viscosity gets reduced due to the presence of elasticity [34]. Thus, in dusty plasmas, a long-lived coherent structure can act as a driving force in order to understand its collective response for a long-time duration without much dissipation.

It is well known that a weakly coupled dusty plasma favors compressible longitudinal modes with usual viscous damping effects. However, in a strongly coupled dusty plasma (SCDP) the strong correlation between the dust grains induces the elasticity to support the incompressible transverse shear (TS) modes in addition to the compressible longitudinal modes [35–37]. This suggests that, below the crystallization limit, a strongly coupled dusty plasma behaves like a viscoelastic fluid. Here, we have modeled such a medium using a well-known phenomenological generalized hydrodynamics (GHD) fluid model which takes into account both types of modes [38,39]. It should be noted that a fluid model focuses on a situation where the spatial scales in dusty plasmas are supposed to be about an order of magnitude larger than the interparticle distance while it fails as soon as the grainy structure becomes important. To study the effect of inhomogeneity on exclusive transverse modes and to avoid the possible coupling with the longitudinal mode, we consider the incompressible limit of the dusty plasma. Theoretically, the existence of transverse modes in the dusty plasma medium has been predicted in [13,14,16]. Schmidt *et al.* [15] showed such transverse modes in molecular dynamics (MD) simulations. Nunomura *et al.* [40], Pramanik *et al.* [41], and Bandyopadhyay

*dharodiv@msu.edu

et al. [42] have also observed transverse modes in dusty plasma experiments. Using the GHD model, the shear waves in a nonuniform dusty plasma have been studied in [43,44]. Apart from the shear waves, a nonuniform dusty plasma under stretching due to a driving force may support the spiral waves. Recently, Kumar *et al.* reported the existence of spiral waves in a dusty plasma at the particle level using MD simulations in [45] and at the continuum level using the GHD model in [46]; in both the studies the medium was driven by an external rotating electric field. In incompressible fluid simulations, Li *et al.* [47] found multiarmed spiral waves in a slowly rotating fluid, driven by a radial unstable temperature gradient. The existence of spiral waves is observed in various biological systems like retinal spreading depression [48], cardiac muscle [49], and Xenopus oocyte calcium waves [50]. Apart from biology, the understanding of spiral waves is important in mathematics and physics, because the spiral wave formation takes place in nonlinear nonequilibrium systems [51]. A rotating galaxy is a good example of large scale spirals [52].

In our previous work [53], we explored the constant density dusty plasmas in an incompressible limit of GHD model and observed the TS waves due to the shear flow induced from a rotating monopole vortex. In the current paper, we use the same model where the smooth and sharp-cutoff rotating vortices are placed at the interface of two incompressible fluids with different densities. The smooth rotating vortex at the interface causes two effects: First, this rotating vortex convects material from the higher density part to the lower density part and vice versa, which leads to the formation of spiral density waves; second, they locally introduce a shear flow. This shear flow is the source for the shear waves. These waves propagate into the surrounding media according to the shear wave speed where the waves travel a smaller distance in the higher density part than in the lower density part in the same time interval. The sharp rotating vortex creates sharp shear flows which favor the KH instability across their interfaces along with the TS waves. In such flows, the interplay between the emitted TS waves and the vortices of KH instability occurs and consequently distorts the formation of the regular spiral density waves around the rotor. Because of the incompressible limit ($\nabla\cdot\vec{v}_d = 0$), to observe the spiral density waves the initial density profile must have a radially varying component to the rotating vortex. Here, the density interface has a tangential discontinuity. This particular situation in 2D dusty plasma experiments represents the coexistence of different density domains with different orientations of the dust grains and the plasmas near the sheath edge or probe, boundary wall, etc. Moreover, the present results can be easily generalized to other SCDP experiments having density inhomogeneity, e.g., sech type and parabolic type.

This paper is organized as follows. In Sec. II, we discuss the incompressible GHD (i-GHD) model and drive an analytical linear wave equation. In Sec. III, we discuss how the simulations are initialized and analyze the dynamical response of the density heterogeneity to the circularly rotating vortex monopoles, particularly, smooth and sharp cutoff. In Sec. III A, we numerically observe that a smooth rotating vorticity profile emits cylindrical TS waves and also causes rolling up of the densities to form the spiral density waves. In Sec. III B, for sharp rotating flows, the interplay between the emitted TS waves and the vortices of KH instability occurs and that, in turn, causes the distortion of the regular spiral density waves around the rotor. Finally, in Sec. IV, we discuss our results and offer concluding remarks.

II. INCOMPRESSIBLE GENERALIZED HYDRODYNAMICS FLUID MODEL

The generalized hydrodynamic fluid model [38,54] is a phenomenological model which is used to study the SCDPs below the crystallization limit, both analytically as well as numerically [38,39,53,55]. The GHD model treats dusty plasma as a viscoelastic fluid in which the coupling strength is proportional to the ratio of η/τ_m [34], and viscosity η in the presence of elasticity τ_m (relaxation time parameter) contributes to the transverse mode due to the strong correlation between dust grains. The parameters η and τ_m are supposed to be empirically related to each other [38,56]. This model supports the existence of both incompressible transverse shear and compressible longitudinal modes. To concentrate on the incompressible features of this system, we separate out the compressibility effects altogether. For this purpose, the i-GHD coupled set of equations has been obtained. In the incompressible limit the Poisson equation is replaced by the quasineutrality condition and charge density fluctuations are ignored. The derivation of the reduced equations has been discussed in detail in earlier papers [53,55] along with the procedure of its numerical implementation and validation. The coupled set of continuity and momentum equations for the dust fluid can be written as

$$\frac{\partial \rho_d}{\partial t} + \nabla\cdot(\rho_d \vec{v}_d) = 0, \tag{1}$$

$$\left[1 + \tau_m\left(\frac{\partial}{\partial t} + \vec{v}_d\cdot\nabla\right)\right] \times \left[\rho_d\left(\frac{\partial \vec{v}_d}{\partial t} + \vec{v}_d\cdot\nabla\vec{v}_d\right) + \nabla p_d + \rho_c\nabla\phi_d\right] = \eta\nabla^2\vec{v}_d, \tag{2}$$

respectively, and the incompressible condition is given as

$$\nabla\cdot\vec{v}_d = 0. \tag{3}$$

Here, $\rho_d = n_d m_d$ is the mass density of the dust fluid (n_d is the number density of dust fluid) and m_d is the mass of the dust particle. The variables ρ_c, $\vec{v}_d$, and ϕ_d are the dust charge density, dust fluid velocity, and dust charge potential, respectively. The pressure p_d term in a strongly coupled plasma is due mainly to the electric field [57]. The time, length, velocity, and potential are normalized by the inverse of dust plasma frequency $\omega_{pd}^{-1} = [4\pi(Z_d e)^2 n_{d0}/m_{d0}]^{-1/2}$ and plasma Debye length $\lambda_d = (K_B T_i/4\pi Z_d n_{d0} e^2)^{1/2}$, $\lambda_d\omega_{pd}$, and $Z_d e/K_B T_i$, respectively. The parameters m_d, T_i, and K_B are the dust grain mass, ion temperature, and Boltzmann constant, respectively. Z_d is the charge on each dust grain with no consideration of charge fluctuation. The number density n_d is normalized by the equilibrium value n_{d0}.

Transverse wave equation

If we take the curl of the above momentum Eq. (2) and keep the linearized terms only, for the moment, the density is constant, i.e., $\rho_d(x, y, t) = \rho_d$, and we immediately get the equation

$$\left[1 + \tau_m \frac{\partial}{\partial t}\right]\left[\frac{\partial \vec{\xi}}{\partial t}\right] = \frac{\eta}{\rho_d}\nabla^2\vec{\xi} \tag{4}$$

where $\vec{\xi} = \vec{\nabla}\times\vec{v}_d$ is the vorticity, normalized with dust plasma frequency. In the limit $\tau_m \frac{\partial}{\partial t} \geqslant 1$, where the memory effects are strong, we get

$$\frac{\partial^2\vec{\xi}}{\partial t^2} = v_p^2\nabla^2\vec{\xi}. \tag{5}$$

This wave, Eq. (5), suggests that the i-GHD model supports the transverse waves moving with phase velocity

$$v_p = \sqrt{\eta/\rho_d\tau_m}. \tag{6}$$

Equation (5) also makes evident that the form of a wave is determined by its source. Let us suppose that we have a line source; the wavefronts will be cylindrical. So, the wave Eq. (5) in cylindrical coordinates will become

$$\frac{\partial^2\xi_z(\vec{r}, t)}{\partial t^2} = v_p^2\left(\frac{\partial^2\xi_z(\vec{r}, t)}{\partial r^2} + \frac{1}{r}\frac{\partial\xi_z(\vec{r}, t)}{\partial r}\right). \tag{7}$$

Here, $r = (x^2 + y^2)^{1/2}$. The solutions are Bessel functions which for large r approach asymptotically [58] to

$$\xi_z(\vec{r}, t) = \xi_z(\vec{r}, \omega) \approx \frac{\vec{\xi_{z0}}}{\sqrt{r}}e^{-j\omega t}. \tag{8}$$

Here, angular frequency $\omega = k\, v_p$ and k is the wave number. The associated wavefronts are cylindrical and propagate radially outward at the phase velocity $v_p = \omega/k = \sqrt{\eta/\rho_d\tau_m}$, and their amplitudes decrease as $1/\sqrt{r}$. If the wavefront emerging or collapsing from or into a point is spherical, its amplitude must attenuate as $1/r$. A planar source will produce plane wavefronts traveling with a constant amplitude, i.e., the wave does not attenuate. The amplitude scaling of these wavefronts is related to the energy conservation consideration. Note that the present simulations have been carried out in two dimensions (the x-y plane), which is the plane of rotation for vorticity structures. So, a numerically expected transverse wave should meet the conditions for the cylindrical case.

III. RESULTS, DISCUSSION, AND NUMERICAL SIMULATION

For the numerical simulation the generalized momentum Eq. (2) has been expressed as a set of the following two coupled convective equations:

$$\rho_d\left(\frac{\partial\vec{v}_d}{\partial t} + \vec{v}_d\cdot\nabla\vec{v}_d\right) + \nabla p_d + \rho_c\nabla\phi_d = \vec{\psi}, \tag{9}$$

$$\frac{\partial\vec{\psi}}{\partial t} + \vec{v}_d\cdot\nabla\vec{\psi} = \frac{\eta}{\tau_m}\nabla^2\vec{v}_d - \frac{\vec{\psi}}{\tau_m}. \tag{10}$$

For our considered 2D system of equations the above variables vary in x and y directions, i.e., $\vec{\psi}(x, y)$, $\vec{v}_d(x, y)$, and $\rho_d(x, y)$. From Eq. (9) it is clear that the quantity $\vec{\psi}(x, y)$ is the strain created in the elastic medium by the time-varying velocity fields. Let us take the curl of Eq. (9). As the curl of a gradient is zero, so the curls of the second and third term (also, we have assumed constant charge density) vanish. Thus, for numerical simulations the final set of coupled model equations (continuity and momentum) becomes

$$\frac{\partial\rho_d}{\partial t} + (\vec{v}_d\cdot\nabla)\rho_d = 0, \tag{11}$$

$$\frac{\partial\vec{\psi}}{\partial t} + (\vec{v}_d\cdot\vec{\nabla})\vec{\psi} = \frac{\eta}{\tau_m}\nabla^2\vec{v}_d - \frac{\vec{\psi}}{\tau_m}, \tag{12}$$

$$\frac{\partial\xi_z}{\partial t} + (\vec{v}_d\cdot\vec{\nabla})\xi_z = \frac{\partial}{\partial x}\left(\frac{\psi_y}{\rho_d}\right) - \frac{\partial}{\partial y}\left(\frac{\psi_x}{\rho_d}\right). \tag{13}$$

We have used the LCPFCT method (Boris *et al.* [59]) to evolve the coupled set of Eqs. (11), (12), and (13) for various kinds of density profiles. This method is based on a finite difference scheme associated with the flux-corrected algorithm. The velocity at each time step has been updated by using Poisson's equation $\nabla^2\vec{v}_d = -\nabla\times\vec{\xi}$. Poisson's equation has been solved by using FISHPACK [60]. It is pointed out that in this particular limit there is nothing specific which suggests that the system corresponds to a strongly coupled dusty plasma. Moreover, it can be applied to other strongly coupled plasma systems as well. Das and Kaw have used the GHD fluid model to model the electron-ion plasma in the context of inertial fusion [61], and Diaw and Murillo applied it to ultracold plasmas and high-energy-density plasmas in [54]. Thus, the reduced set of equations not only caters to the strongly coupled incompressible dusty plasma medium but is also relevant for any other incompressible strongly coupled system. Numerically, in order to understand the dynamical response of density inhomogeneous SCDPs, we consider two cases of a circularly rotating fluid vortex, especially having (A) a smooth rotating vortex and (B) a sharp cutoff. Boundary conditions are periodic along the x axis while nonperiodic along the vertical (y-axis) direction where the effects of perturbed quantities die out before hitting the boundary of the simulation box. For all cases the sharp inhomogeneity in density has been introduced along the interface $y = 0$. Here, it should be noted that this initial condition has nothing to

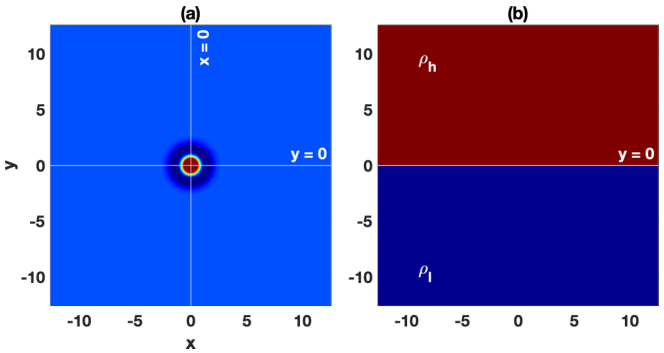

FIG. 1. The initial smooth vorticity and density profiles. (a) Smooth rotating vorticity profile given by Eq. (14). (b) Density profile where the lighter fluid is positioned side by side to the denser fluid along the $y = 0$ interface.

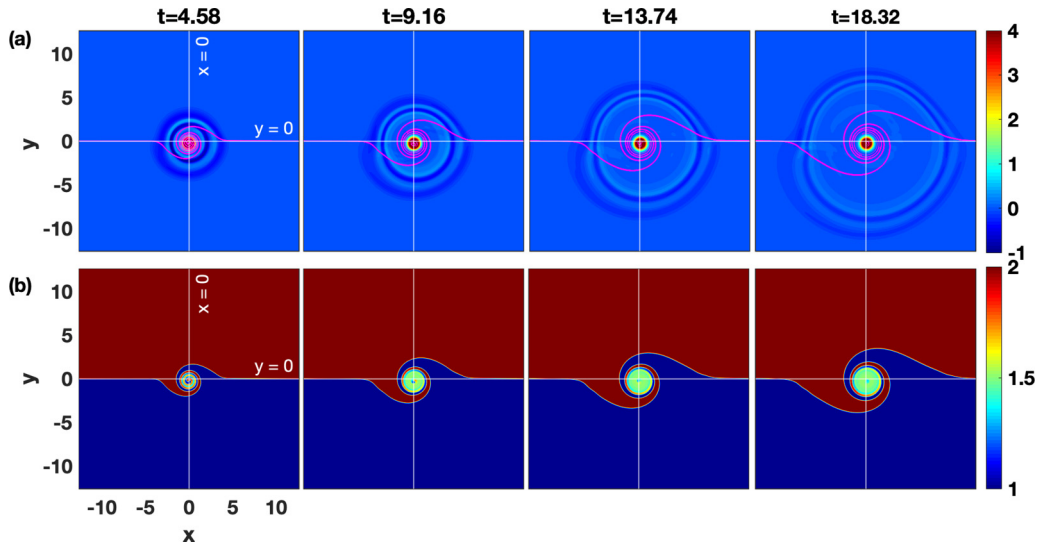

FIG. 2. The inhomogeneous viscoelastic fluid has η=5 and τ_m=20. (a) Time evolution of a counterclockwise rotating vorticity profile ($\Omega_0 = 10$) [Fig. 1(a)]; the magenta solid line over the vorticity profile represents the interface of the respective density evolution to the vorticity; the colorbar indicates the vorticity. (b) Density profile evolution [Fig. 1(b)]; the colorbar indicates the density (see Supplemental Material [62]).

do with the Rayleigh-Taylor instability as our system has no density stratification against an accelerating force like gravity.

A. Smooth rotating vortex

In the former case (A), we have considered a system of length $lx = ly = 8\pi$ units with a sharp interface of density heterogeneity shown in Fig. 1(b), where two incompressible fluids with different constant densities $\rho_l = 1$ for $-4\pi \leqslant y \leqslant 0$ (lower half) and $\rho_h = 2$ for $0 \leqslant y \leqslant 4\pi$ (upper half) are positioned side by side along the $y = 0$ interface.

In the interest of density waves and vorticity evolution, the sharp density interface of the medium has been perturbed through a counterclockwise rotating vorticity structure centered at $(x, y) = (0, 0)$, given by

$$\xi_{z0}(x, y, t_0) = \Omega_0[1 - (x^2 + y^2)]\exp[-(x^2 + y^2)], \qquad (14)$$

having the velocity components which satisfy the condition of incompressibility $\nabla\cdot\vec{v}_d = 0$ using $\vec{\xi} = \nabla\times\vec{v}_d$, $v_{dx0}(x, y, t_0) = -\phi_0 y\exp[-(x^2 + y^2)]$, and $v_{dy0}(x, y, t_0) = \phi_0 x\exp[-(x^2 + y^2)]$. Here $\Omega_0 = 2\phi_0$ is proportional to the total circulation. This vorticity profile has circular symmetry [Fig. 1(a)].

1. Transverse shear waves

Figure 2(a) shows the time evolution of the above discussed smooth vorticity profile ($\Omega_0 = 10$) in an inhomogeneous viscoelastic fluid [Fig. 2(b)] which has the coupling parameter values $\eta = 5$ and $\tau_m = 20$.

From Fig. 2(a), as soon as the vortex starts rotating at the interface it induces two effects: First, the densities are rolled up to form the spiral density waves (we will discuss this later); second, they locally introduce a shear flow. This shear flow is the source for the radial shear waves. These radial waves travel a smaller distance in the higher density side (upper half) than in the lower density side (lower half) in the same time interval or the waves are slower in the denser side. In the interest of speed of these outgoing shear waves we have plotted the position vs time of a particular wavefront in Fig. 3 along the y axis for $x = 0$. In Fig. 3, the position-time slope suggests that the phase velocity (v_p) is found to match with Eq. (6), i.e., $v_p \approx 0.35$ for the denser side ($\eta = 5$; $\tau_m = 20$ and $\rho_h = 2$ for $y > 0$) and in the lighter side $v_p \approx 0.5$ ($\eta = 5$; $\tau_m = 20$ and $\rho_l = 1$ for $y < 0$). *This confirms that the outgoing waves are the TS waves.*

Figure 4 shows the radial fall of amplitudes of the TS waves in both halves (denser and lighter) of the density profile. It is found to match the fall of amplitude with $1/\sqrt{|y|}$, which meets the requirement of energy conservation for a cylindrical wave (this has been discussed in Sec. II). *This confirms that the outgoing TS waves have cylindrical shape in both halves.*

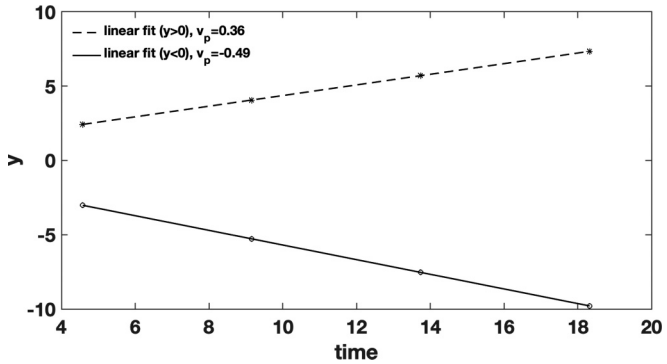

FIG. 3. Position-time graph of the radially propagating wavefronts (along the y axis for $x = 0$) observed in Fig. 2(a). v_p is the phase velocity (slope of the position-time plot). The radial wave travels faster ($v_p \approx 0.5$) in the lower half ($y < 0$) and slower ($v_p \approx 0.35$) in the upper half ($y > 0$) of the medium, which satisfies Eq. (6). It confirms that the outgoing waves are the transverse shear waves.

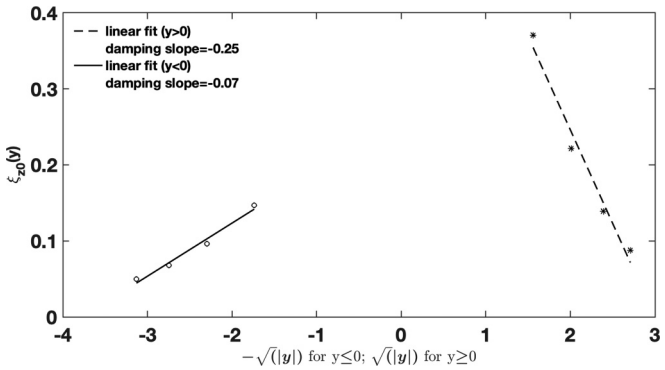

FIG. 4. Amplitude vs square root of the position of a radially propagating wavefront along the y axis for $x = 0$ [Fig. 2(a)]. The amplitude of a wavefront decreases as $1/\sqrt{|y|}$. It confirms that the emitted TS waves have cylindrical shape.

Hence, both the above observations (Figs. 3 and 4) confirm that these outgoing waves are the linear cylindrical TS waves as suggested by analytical Eq. (7) and also indicate the validation of our numerical code. Figure 5 shows that the late-time snapshot of a counterclockwise rotating vorticity profile has the same value of total circulation $\Omega_0 = 10$ in different media; each has a lower half for $-4\pi \leqslant y \leqslant 0$ and an upper half for $0 \leqslant y \leqslant 4\pi$. The left and the middle snapshots show the vorticity vortex in the inviscid hydrodynamic (HD) fluid and in the viscoelastic fluid (η= 5 and $\tau_m = 20$), respectively; both have the same density inhomogeneity $\rho_l = 1$ for the lower half and $\rho_h = 2$ for the upper half. Radial waves travel faster in the lower half ($\rho_l = 1$) than in the upper half ($\rho_h = 2$). This difference in speeds of the waves induces a net radial flow of the medium in the downward direction which can be noticed as a downward shift of the vortex center in Fig. 5(b) while the HD fluid, on the other hand, does not support any TS wave so no shifting is observed as shown in Fig. 5(a).

Figure 5(c) represents another viscoelastic fluid ($\eta = 5$ and $\tau_m = 20$) which has the same density in the lower half as in Fig. 5(b), i.e., $\rho_l = 1$, while the upper half is denser ($\rho_h = 4$) in Fig. 5(c) than $\rho_h = 2$ in Fig. 5(b). Thus, the TS waves are supposed to travel at the same speed in the lower halves of both fluids while in the upper halves the speed of TS waves is higher in Fig. 5(b) than in Fig. 5(c). All these observations suggest that the net flow of the medium is supposed to be larger in the downward direction in Fig. 5(c) than in Fig. 5(b). This is observed in terms of the larger shift of the vortex center in the downward direction in Fig. 5(c) than in Fig. 5(b). A closer look [Figs. 5(a) and 5(b)] shows that the density gradient and net relative velocity cause a small horizontal right shift of the vortex center along with the downward vertical shift. Furthermore, the density gradient and the unequal velocities make the cylindrical waves asymmetric to the center of rotation. The coupling strength parameter Γ for a dusty plasma is proportional to the cube root of the density [63], which means the denser side has a larger coupling strength than the lighter one. This effect can be noticed from Figs. 2(a), 5(b), and 5(c), where the TS waves get clearer and steeper in the denser side (upper half) than in the lighter one (lower half).

2. *Formation and evolution of spiral density waves*

After the confirmation of TS waves, let us focus on the evolution of the background density profile shown in Fig. 2(b), where the rotating vortex basically convects material from the higher denser part to the less dense part and vice versa, which results in the spiral density arms or waves around the vortex with time. One of the main advantages of viscoelastic fluids is that a rotating vortex in such media can drive density waves for a long-time duration without much dissipation compared with hydrodynamic fluids. A comparative analysis of the vorticity evolution in Fig. 2(a) to the density evolution in Fig. 2(b) shows that the perturbed density region along the interface $y = 0$ follows the radially propagating TS waves and remains confined within the distance traveled by the TS waves at that moment. To make it more clear we have also plotted the interface of the respective density profile over the vorticity using a magenta colored solid line in Fig. 2(a). In order to substantiate the observation in Fig. 2, we have also simulated two more cases with the same background density inhomogeneity: first [Fig. 6(a)] with the same rotation rate of vorticity ($\Omega_0 = 10$) but with different values of coupling parameters ($\eta = 2.5$; $\tau_m = 20$), i.e., TS waves travel with less phase velocity, and second [Fig. 6(b)] with double the

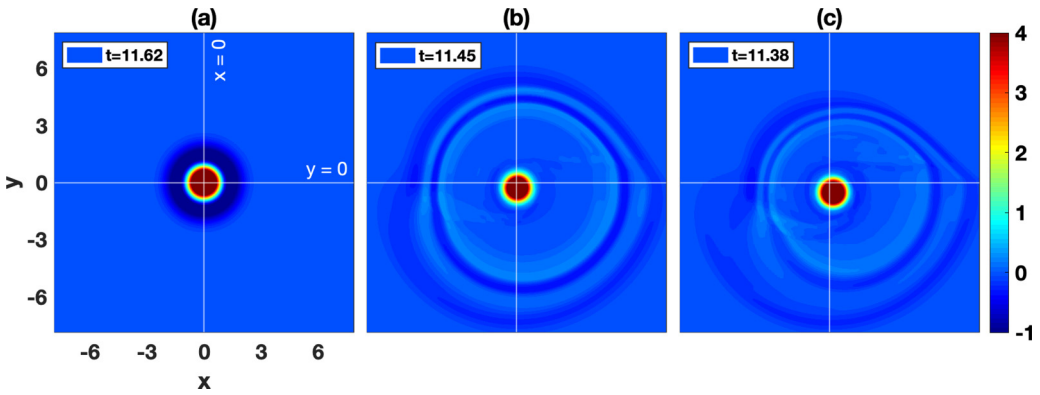

FIG. 5. Late-time snapshots of a counterclockwise rotating vorticity profile ($\Omega_0 = 10$) in different media: Panels (a) and (b) depict density inhomogeneity, $\rho_l = 1$ for $-4\pi \leqslant y \leqslant 0$ and $\rho_h = 2$ for $0 \leqslant y \leqslant 4\pi$, while panel (c) depicts the same density value in the lower half as in panels (a) and (b), i.e., $\rho_l = 1$, but the upper half is more dense, i.e., $\rho_h = 4$. The shift of the vortex center in the downward direction can be observed to be larger in panel (c) than in panel (b) because the TS waves are slower in the denser medium. (a) An inviscid HD fluid does not support any TS wave so no shifting is observed.

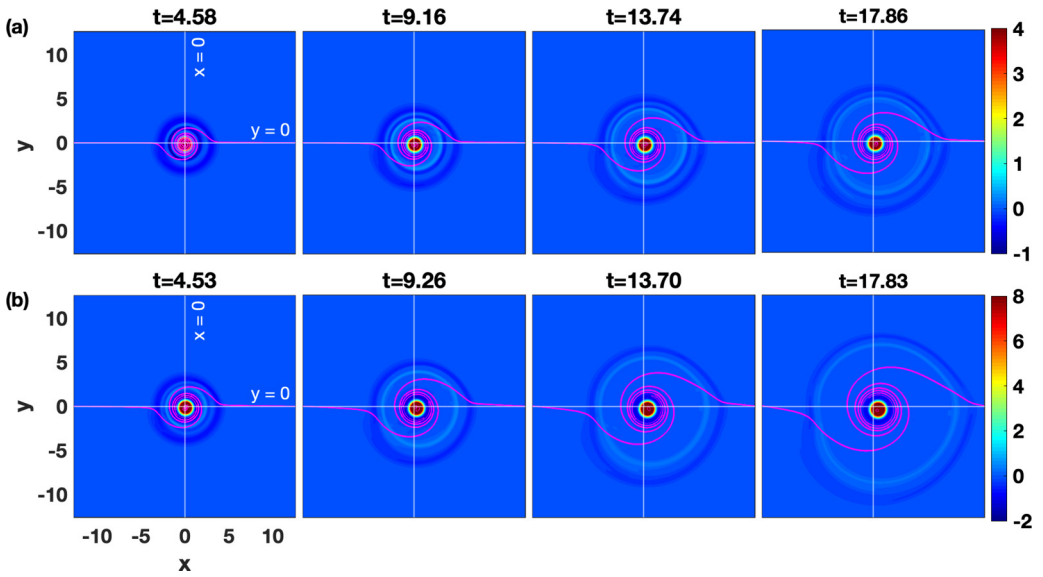

FIG. 6. Time evolution of the rotating vorticity profiles in the viscoelastic fluids with the same density inhomogeneity as in Fig. 2(b), where the solid line (magenta color) over the rotating vortices represents the evolution of the respective density interface. In panel (a) vorticity has $\Omega_0 = 10$ and the fluid has the values of coupling parameters η= 2.5 and τ_m=20, and in panel (b) vorticity has $\Omega_0 = 20$ and the fluid has the values of coupling parameters η= 5 and τ_m=20. It is observed that the perturbed density region along the interface follows the radially propagating TS waves and remains confined within them.

rotation rate of vorticity ($\Omega_0 = 20$) but with the same values of coupling parameters ($\eta = 5$ and $\tau_m = 20$), i.e., TS waves travel with the same phase velocity [Fig. 2(a)]. It can be seen that these two cases too favor our earlier observation that the perturbed density region along the interface $y = 0$ follows the TS waves. This means the spiral waves can be controlled by tweaking the coupling parameter values.

Some other interesting observations can be visualized more clearly through the zoomed density contour snapshots shown in Fig. 7.

Spiral waves have both angular as well as radial velocity components. A comparison between Fig. 7(a) ($\Omega_0 = 10$) and Fig. 7(b) ($\Omega_0 = 20$) shows that the expansion rate (radial component) is high and the number of turns (angular component) of the spiral arms is almost double in Fig. 7(b) in comparison to Fig. 7(a) due to the factor 2 angular velocity. Thus, the conclusion is that the number of turns of spiral arms is proportional to the amplitude of vorticity. Furthermore, the spiral arms of both densities (lighter and denser) are distinguishable in the early time while later they get smeared out. So

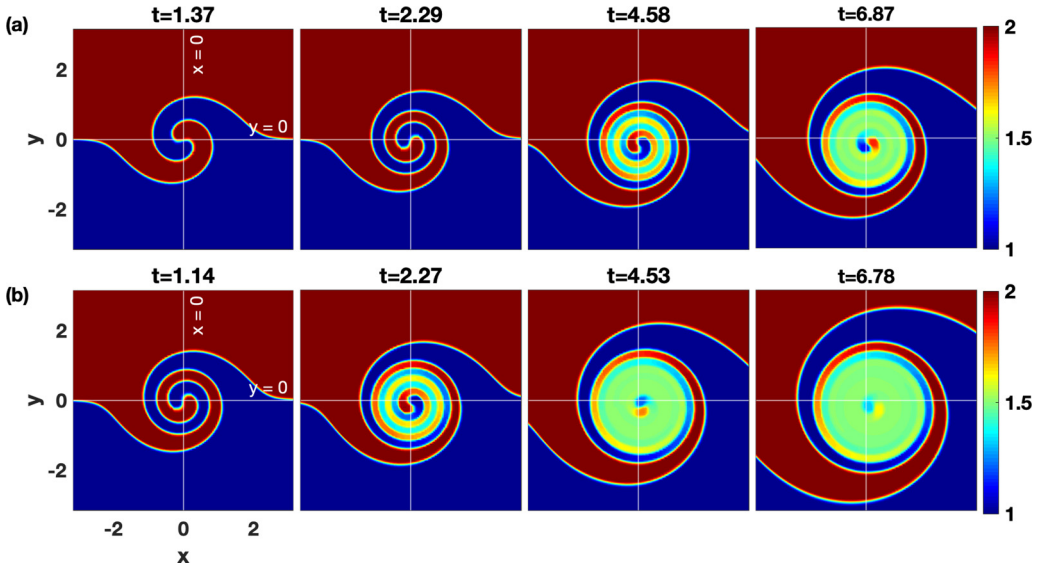

FIG. 7. Time evolution of the sharp density profile for viscoelastic fluid with $\eta = 5$ and $\tau_m = 20$. In panel (a) vorticity has $\Omega_0 = 10$ and in panel (b) vorticity has $\Omega_0 = 20$. The expansion rate (radial velocity) is high and the number of turns (angular velocity) of the spiral arms is almost double in panel (b) in comparison to panel (a) due to the factor 2 angular velocity. Furthermore, the spiral arms of both densities (lighter and denser) are distinguishable in the early time while later they get smeared out.

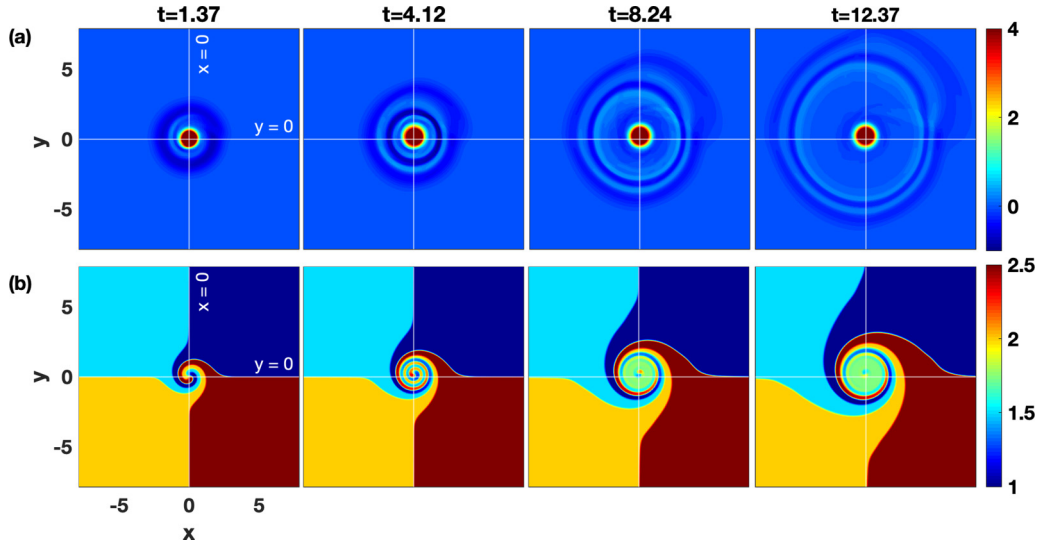

FIG. 8. Four viscoelastic fluids ($\eta = 5$ and $\tau_m = 20$) of different densities over the smooth rotating vortex. (a) Time evolution of vorticity. It can be noticed that the greater the density/Γ of the medium the steeper the TS waves; the lighter the density of a medium, the faster the speed of the TS waves; the speed difference in different quadrants and the density gradient cause the wavefronts to be not cylindrically symmetric; and there is a shift in the vorticity center towards the low density quadrant; the colorbar designates the rotating vorticity. (b) Time evolution of four different sharp density profiles: four distinguishable spiral arms for each density are observed in the early time while later they get smeared out; the colorbar shows the density.

far, we have dealt with a medium having two fluids of different densities, which results in the formation of two kinds of spiral arms. A medium in nature can also exist more than two fluids with different densities. We consider, therefore, that a medium has four fluids of different densities ($\rho_d = 1$, 1.5, 2, and 2.5) over the rotating coherent structure as shown in Fig. 8. The boundary conditions have been taken care of by considering that all the four density quadrants are localized and lie inside the density region considered in Fig. 1(b).

Figure 8 depicts some of the same observations as made previously: The greater the density/Γ of the medium, the steeper the TS waves; the lighter the density of a medium, the faster the speed of TS waves; the speed difference in different quadrants and the density gradient cause the wavefronts to be not cylindrically symmetric around the center of rotation; and the shift in the vorticity center follows the density gradient. In Fig. 8(b) four distinguishable spiral arms for each density are observed in the early time while later they get smeared out.

Thus, from all the above evolutions of the density profiles it can be anticipated that the number of spiral arms is proportional to the number of different densities that coexist over the smooth rotating structure.

B. Sharp rotating vortex

In an earlier subsection, we had specifically avoided the formation of Kelvin-Helmholtz instability by taking a smooth flow profile. In this subsection, we consider the vorticity profile B with a sharp cutoff [first snapshot at $t = 0$ in Figs. 9(a) and 10(a)], i.e., we set the vorticity $\xi_{z0} = 0$ beyond $r = r_0$ ($= 6.0$) and for $r \leqslant r_0$ the vorticity is taken to have a constant value $\xi_{z0} = 2\phi_0$ and $\phi_0 = 1$. Another possibility which we explored in our previous paper [53] was the evolution of the same sharp-cutoff rotating vortex in viscoelastic fluids with constant background density. In the present paper, we introduce an additional density inhomogeneity where $\rho_l = 1$ (lower half) for $-6\pi \leqslant y \leqslant 0$ and $\rho_h = 2$ (upper half) for $0 \leqslant y \leqslant 6\pi$ [first snapshot at $t = 0$ in Figs. 9(b) and 10(b)]. For the HD system, it is evident from Fig. 9 that in turning on the vortex the steepness of the vorticity profile generates a strong rotational sheared flow which results in creation of small KH vortices across the vorticity interface and after that as time progresses the merging of these vortices takes place. This creation and merging process of KH vortices distorts the rolling process of the background density around the rotor, which results in formation of deformed spiral density waves around it.

Based on the observations thus far, we can anticipate that a rigid rotor in an incompressible viscoelastic fluid, besides KH instability, would also support the TS wave emission. In Fig. 10(a) where $\eta = 5$ and $\tau_m = 20$, we observe a pair of ingoing and outgoing wavefronts emanating from the interface and a concomitant KH destabilization at each of these fronts. The response of the respective background fluid density to the rigid rotor [Fig. 10(a)] is shown in Fig. 10(b), where as soon as the rotor begins to rotate, initially, the fluid within the inner region ($|r| \leqslant 6$) starts rotating with it, which later undergoes mixing due to the ingoing wave from the interface, while the stagnant fluid in the outer region ($|r| \geqslant 6$) undergoes mixing due to the outgoing wave from the interface. Thus, the TS waves assist the process of fluid mixing by convecting the fluids inside and outside the vortex structure. The fluid near the interface starts binding around it. The interplay between the ingoing and outgoing wavefronts and KH instability distorts the formation of regular spiral waves around the rotor. Again, a vorticity vortex shift towards the low density side is observed while no shifting is observed for hydrodynamic fluid.

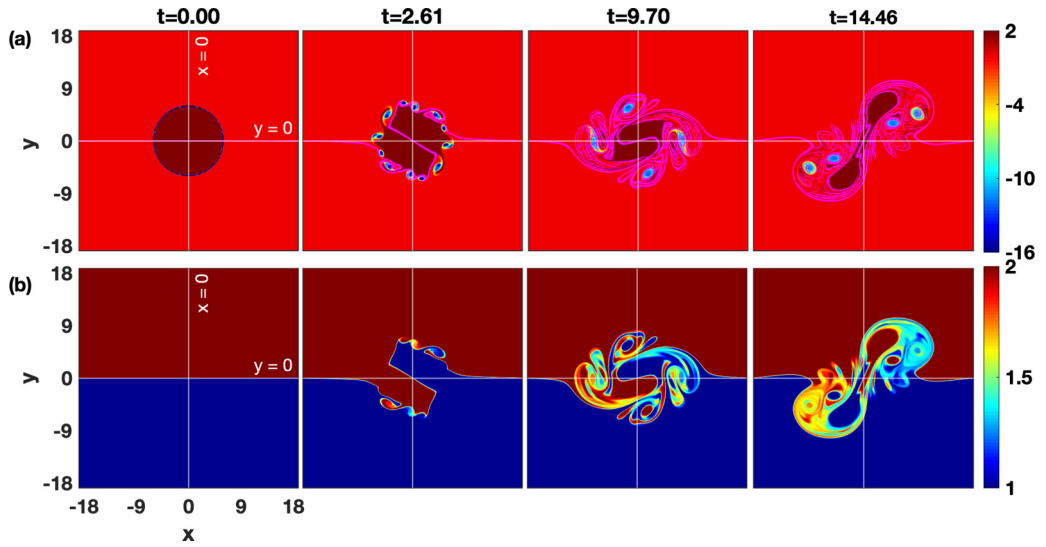

FIG. 9. An inviscid HD fluid. (a) The time evolution of a sharp counterclockwise rotating vorticity profile ($\Omega_0 = 2$): The steepness of the vorticity profile generates small KH vortices across its interface. (b) Density evolution: The creation and merging process of KH vortices distort the formation of the regular spiral waves around the rotor. In panel (a) the magenta solid line over the vorticity profile represents the interface of the respective density evolution to the vorticity.

In Fig. 11, we have simulated another case of viscoelastic fluid with the same density inhomogeneity but with different values of coupling parameters η= 2.5 and τ_m=20, i.e., TS waves have less phase velocity than in Fig. 11. A comparative analysis of Figs. 10 and 11 shows that the higher phase velocity of the TS waves assists the medium to evolution towards an isotropic structure much faster, and promotes the mixing and diffusion processes more quickly.

It should be noted that, in this paper, the HD results are used only to facilitate the understanding of our observations of viscoelastic fluids, not for any comparative analysis.

IV. CONCLUSIONS AND OUTLOOK

Strongly coupled dusty plasmas support long-lived coherent structures, which can provide a driving force for the generation of different types of waves and instabilities. Here, we have examined how density heterogeneity in the incompressible limit of SCDPs responds to the rotating vortex monopoles, particularly, smooth and sharp cutoff. The SCDPs have been treated as viscoelastic fluids. Two-dimensional fluid simulations have been carried out in the framework of the i-GHD model. The rotating vortices are placed at the interface of different densities. Some main observations are as follows.

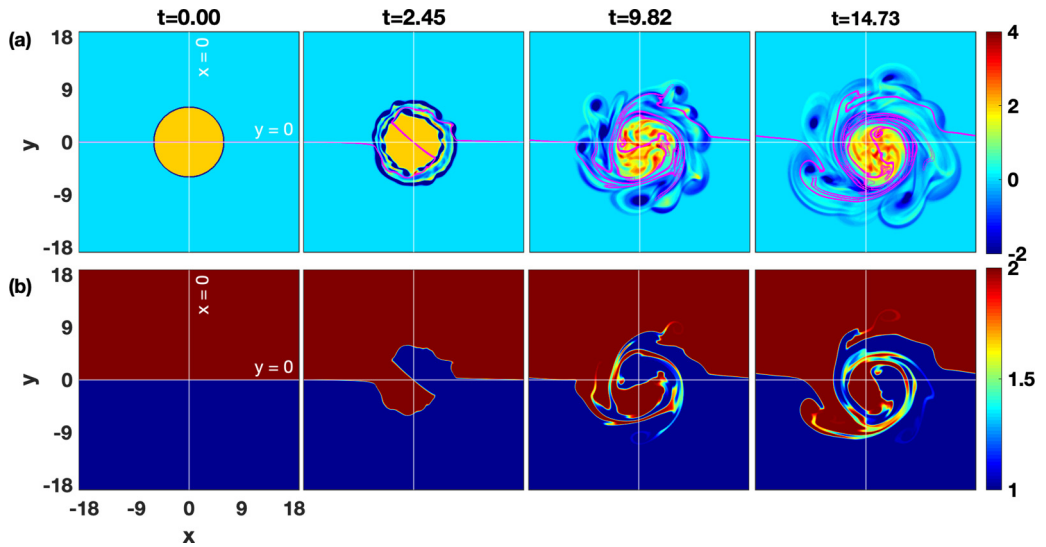

FIG. 10. Viscoelastic fluid with coupling parameters $\eta = 5$ and $\tau_m = 20$. (a) The time evolution of a sharp counterclockwise rotating vorticity profile ($\Omega_0 = 2$): A pair of ingoing and outgoing wavefronts emanates from the interface and a concomitant KH destabilization at each of these fronts. (b) Density evolution: The interplay between the ingoing and outgoing wavefronts and KH instability perverts the formation of regular spiral waves around the rotor. In panel (a) the magenta solid line over the vorticity profile represents the interface of the respective density evolution to the vorticity.

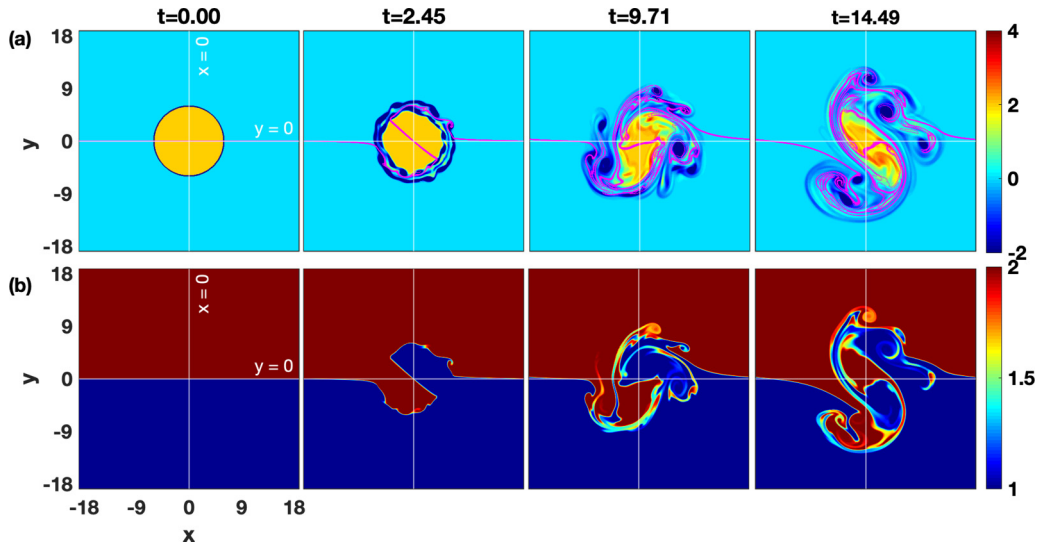

FIG. 11. Viscoelastic fluid with coupling parameters $\eta = 2.5$ and $\tau_m = 20$. (a) The time evolution of a sharp counterclockwise rotating vorticity profile ($\Omega_0 = 2$): A pair of ingoing and outgoing wavefronts emanates from the interface and a concomitant KH destabilization at each of these fronts. (b) Density evolution: The interplay between the ingoing and outgoing wavefronts and KH instability perverts the formation of regular spiral waves around the rotor. In panel (a) the magenta solid line over the vorticity profile represents the interface of the respective density evolution to the vorticity.

(1) A smooth rotating vortex drives the spiral density waves and shear in flow. The shear flow induces the TS waves into the surrounding media.

(2) The shear waves move slower in the denser side and faster in the lighter side. The difference in speeds of the waves induces a net radial flow of the medium towards the lower density side, which can be noticed as a shift of the vortex center in the direction of the density gradient.

(3) The number of spiral arms is proportional to the number of different densities that coexist over the smooth rotating structure.

(4) The spiral density waves are distinguishable in the early time while later they get smeared out. Spiral waves are observed in many biological, physical, and chemical systems [64–68].

(5) A sharp rotating vortex favors KH instability across its interface. In such flows, the interplay between the emitted TS waves and the vortices of KH instability distorts the formation of the regular spiral density arms around the rotor.

(6) By tweaking the coupling parameter values, in the case of a smooth profile the impact of spiral density waves can be controlled. In the sharp rotating vortex, transport properties like mixing and diffusion can be controlled.

(7) An inviscid HD fluid does not support any TS wave so no shifting is observed to the vortex center due to the density inhomogeneity.

(8) Density inhomogeneity and the speed variation of shear waves cause asymmetry in the emergent cylindrical wavefront.

(9) The coupling strength of a dusty plasma is proportional to the cube root of the density, which means the denser side has a larger coupling strength than the lighter one. So, in vorticity plots, the TS waves get clearer and steeper in the denser side than in the lighter one.

We believe these results can inspire future experiments. Here, the density inhomogeneity has a tangential discontinuity. This discontinuity is very common in almost all branches of the physical sciences. This particular situation in 2D dusty plasma experiments represents the coexistence of different density domains with different orientations of the dust grains and the plasmas near the sheath edge or probe, boundary wall, etc. Moreover, the presented results can be easily generalized to other SCDP experiments having density inhomogeneity, e.g., sech type and parabolic type.

In a three-dimensional system the TS waves may be less effective because the amplitude of an emerging TS wave from a spherical source will decrease faster $(1/r)$ than in the present 2D case (here, $1/\sqrt{r}$). It would also be interesting to see the evolution of such inhomogeneous media having other types of coherent structures like elliptical, dipole, and tripole. Furthermore, the inclusion of compressibility in the present model will make the considered system closer to a real dusty plasma, where it will be interesting to see how the energy exchange takes place between both modes and how the new emerging waves control the expansion and roll of spiral waves. In single component 2D SCDPs, the transfer of energy between both the modes has been studied in [69].

ACKNOWLEDGMENTS

The author would like to thank the Prof. Michael S. Murillo (CMSE, MSU) for his motivation during the preparation this manuscript. The author also wish to thank Dr. Deepak Sangwan, Dr. Mangilal Choudhary, and Dr. Neeraj Chaubey for very useful feedback on the manuscript.

[1] A. Tur and V. Yanovsky, *Coherent Vortex Structures in Fluids and Plasmas* (Springer, New York, 2017).

[2] L. F. Rossi, J. F. Lingevitch, and A. J. Bernoff, Quasi-steady monopole and tripole attractors for relaxing vortices, Phys. Fluids **9**, 2329 (1997).

[3] Z. Kizner and R. Khvoles, The tripole vortex: Experimental evidence and explicit solutions, Phys. Rev. E **70**, 016307 (2004).

[4] T. Leweke, S. Le Dizès, and C. H. K. Williamson, Dynamics and instabilities of vortex pairs, Ann. Rev. Fluid Mech. **48**, 507 (2016).

[5] M. J. Lighthill and J. Lighthill, *Waves in Fluids* (Cambridge University, Cambridge, England, 2001).

[6] N. N. Rao, P. K. Shukla, and M. Yu. Yu, Dust-acoustic waves in dusty plasmas, Planetary and Space Science **38**, 543 (1990).

[7] M. Choudhary, S. Mukherjee, and P. Bandyopadhyay, Propagation characteristics of dust–acoustic waves in presence of a floating cylindrical object in the dc discharge plasma, Physics of Plasmas **23**, 083705 (2016).

[8] J. Grove, The interaction of shock waves with fluid interfaces, Adv. Appl. Math. **10**, 201 (1989).

[9] D. Rotman, Shock wave effects on a turbulent flow, Phys. Fluids A **3**, 1792 (1991).

[10] W. Lin, M. S. Murillo, and Y. Feng, Pressure and energy of compressional shocks in two-dimensional Yukawa systems, Phys. Rev. E **100**, 043203 (2019).

[11] S. Imao, M. Itoh, Y. Yamada, and Q. Zhang, The characteristics of spiral waves in an axially rotating pipe, Experiments in Fluids **12**, 277 (1992).

[12] D. Barkley, Linear Stability Analysis of Rotating Spiral Waves in Excitable Media, Phys. Rev. Lett. **68**, 2090 (1992).

[13] F. M. Peeters and Xiaoguang Wu, Wigner crystal of a screened-Coulomb-interaction colloidal system in two dimensions, Phys. Rev. A **35**, 3109 (1987).

[14] S. V. Vladimirov, P. V. Shevchenko, and N. F. Cramer, Vibrational modes in the dust-plasma crystal, Phys. Rev. E **56**, R74 (1997).

[15] P. Schmidt, G. Zwicknagel, P.-G. Reinhard, and C. Toepffer, Longitudinal and transversal collective modes in strongly correlated plasmas, Phys. Rev. E **56**, 7310 (1997).

[16] X. Wang, A. Bhattacharjee, and S. Hu, Longitudinal and Transverse Waves in Yukawa Crystals, Phys. Rev. Lett. **86**, 2569 (2001).

[17] M. S. Murillo, Critical Wave Vectors for Transverse Modes in Strongly Coupled Dusty Plasmas, Phys. Rev. Lett. **85**, 2514 (2000).

[18] B. Liu, K. Avinash, and J. Goree, Transverse optical mode in a one-dimensional Yukawa chain, Phys. Rev. Lett. **91**, 255003 (2003).

[19] P. G. Drazin, Kelvin-Helmholtz instability of finite amplitude, J. Fluid Mech. **42**, 321 (1970).

[20] S. Chandrasekhar, *Hydrodynamic and Hydromagnetic Stability* (Dover, New York, 1981).

[21] L. Rayleigh, Investigation of the character of the equilibrium of an incompressible heavy fluid of variable density, in *Scientific Papers*, Vol.II (Cambridge Univ. Press, 1900), pp. 200–207.

[22] G. I. Taylor, The instability of liquid surfaces when accelerated in a direction perpendicular to their planes, I, Proc. R. Soc. London, Ser. A **201**, 192 (1950).

[23] H. Thomas, G. E. Morfill, V. Demmel, J. Goree, B. Feuerbacher, and D. Möhlmann, Plasma Crystal: Coulomb Crystallization in a Dusty Plasma, Phys. Rev. Lett. **73**, 652 (1994).

[24] E. Thomas, Jr., Direct measurements of two-dimensional velocity profiles in direct current glow discharge dusty plasmas, Physics of Plasmas **6**, 2672 (1999).

[25] R. Ichiki, Yu. Ivanov, M. Wolter, Y. Kawai, and A. Melzer, Melting and heating of two-dimensional Coulomb clusters in dusty plasmas, Phys. Rev. E **70**, 066404 (2004).

[26] Z. Haralson and J. Goree, Laser heating of 2-D dusty plasmas using a random arc pattern, IEEE Transactions on Plasma Science **44**, 549 (2015).

[27] Z. Haralson and J Goree, Temperature dependence of viscosity in a two-dimensional dusty plasma without the effects of shear thinning, Physics of Plasmas **23**, 093703 (2016).

[28] A. Melzer, H. Krueger, S. Schuett, and M. Mulsow, Finite dust clusters under strong magnetic fields, Physics of Plasmas **26**, 093702 (2019).

[29] A. Kananovich and J. Goree, Experimental determination of shock speed versus exciter speed in a two-dimensional dusty plasma, Phys. Rev. E **101**, 043211 (2020).

[30] A. Piel, V. Nosenko, and J. Goree, Laser-excited shear waves in solid and liquid two-dimensional dusty plasmas, Physics of Plasmas **13**, 042104 (2006).

[31] Y. Feng, W. Lin, W. Li, and Q. Wang, Equations of state and diagrams of two-dimensional liquid dusty plasmas, Physics of Plasmas **23**, 093705 (2016).

[32] P. Hartmann, J. C. Reyes, E. G. Kostadinova, L. S. Matthews, T. W. Hyde, R. U. Masheyeva, K. N. Dzhumagulova, T. S. Ramazanov, T. Ott, H. Kahlert, M. Bonitz, I. Korolov, and Z. Donko, Self-diffusion in two-dimensional quasimagnetized rotating dusty plasmas, Phys. Rev. E **99**, 013203 (2019).

[33] W. Lin, M. S. Murillo, and Y. Feng, Universal relationship of compression shocks in two-dimensional Yukawa systems, Phys. Rev. E **101**, 013203 (2020).

[34] J. Frenkel, *Kinetic Theory Of Liquids* (Dover, New York, 1955).

[35] S. Nunomura, J. Goree, S. Hu, X. Wang, and A. Bhattacharjee, Dispersion relations of longitudinal and transverse waves in two-dimensional screened Coulomb crystals, Phys. Rev. E **65**, 066402 (2002).

[36] S. Nunomura, S. Zhdanov, D. Samsonov, and G. Morfill, Wave Spectra in Solid and Liquid Complex (Dusty) Plasmas, Phys. Rev. Lett. **94**, 045001 (2005).

[37] I. Donkó, Peter Hartmann, and Z. Donkó, Molecular dynamics simulation of a two-dimensional dusty plasma, Am. J. Phys. **87**, 986 (2019).

[38] P. K. Kaw and A. Sen, Low frequency modes in strongly coupled dusty plasmas, Physics of Plasmas **5**, 3552 (1998).

[39] P. K. Kaw, Collective modes in a strongly coupled dusty plasma, Physics of Plasmas **8**, 1870 (2001).

[40] S. Nunomura, D. Samsonov, and J. Goree, Transverse Waves in a Two-Dimensional Screened-Coulomb Crystal (Dusty Plasma), Phys. Rev. Lett. **84**, 5141 (2000).

[41] J. Pramanik, G. Prasad, A. Sen, and P. K. Kaw, Experimental Observations of Transverse Shear Waves in Strongly Coupled Dusty Plasmas, Phys. Rev. Lett. **88**, 175001 (2002).

[42] P. Bandyopadhyay, G. Prasad, A. Sen, and P. K. Kaw, Driven transverse shear waves in a strongly coupled dusty plasma, Phys. Lett. A **372**, 5467 (2008).

[43] A. Mishra, P. K. Kaw, and A. Sen, Instability of shear waves in an inhomogeneous strongly coupled dusty plasma, Physics of Plasmas **7**, 3188 (2000).

[44] G. Sorasio, P. K. Shukla, and D. P. Resendes, Instability of shear waves in a nonuniform dusty plasma, New Journal of Physics **5**, 81 (2003).

[45] S. Kumar and A. Das, Spiral waves in driven strongly coupled Yukawa systems, Phys. Rev. E **97**, 063202 (2018).

[46] S. Kumar, B. Patel, and A. Das, Spiral waves in driven dusty plasma medium: Generalized hydrodynamic fluid description, Physics of Plasmas **25**, 043701 (2018).

[47] L. Li, X. Liao, K. H Chan, and K. Zhang, On nonlinear multiarmed spiral waves in slowly rotating fluid systems, Phys. Fluids **22**, 011701 (2010).

[48] N. A. Gorelova and J. Bureš, Spiral waves of spreading depression in the isolated chicken retina, Journal of Neurobiology **14**, 353 (1983).

[49] J. M. Davidenko, A. V. Pertsov, R. Salomonsz, W. Baxter, and J. Jalife, Stationary and drifting spiral waves of excitation in isolated cardiac muscle, Nature (London) **355**, 349 (1992).

[50] J. Lechleiter, S. Girard, E. Peralta, and D. Clapham, Spiral calcium wave propagation and annihilation in xenopus laevis oocytes, Science **252**, 123 (1991).

[51] H. Kitahata and M. Tanaka, Mathematical approach to unpinning of spiral waves anchored to an obstacle with high-frequency pacing, Biophysics physicobiology **15**, 196 (2018).

[52] D. M. Elmegreen, A near-infrared atlas of spiral galaxies, The Astrophys. J. Suppl. Ser. **47**, 229 (1981).

[53] V. S. Dharodi, S. K. Tiwari, and A. Das, Visco-elastic fluid simulations of coherent structures in strongly coupled dusty plasma medium, Physics of Plasmas **21**, 073705 (2014).

[54] A. Diaw and M. S. Murillo, Generalized hydrodynamics model for strongly coupled plasmas, Phys. Rev. E **92**, 013107 (2015).

[55] V. S. Dharodi, A. Das, B. G. Patel, and P. K. Kaw, Sub-and super-luminar propagation of structures satisfying Poynting-like theorem for incompressible generalized hydrodynamic fluid model depicting strongly coupled dusty plasma medium, Physics of Plasmas **23**, 013707 (2016).

[56] S. Ichimaru, H. Iyetomi, and S. Tanaka, Statistical physics of dense plasmas: thermodynamics, transport coefficients and dynamic correlations, Phys. Rep. **149**, 91 (1987).

[57] T. M. Flanagan and J. Goree, Observation of the spatial growth of self-excited dust-density waves, Physics of Plasmas **17**, 123702 (2010).

[58] N. Sekeljic, Asymptotic expansion of bessel functions; applications to electromagnetics, Dynamics at the Horsetooth, 2A, 2010.

[59] J. P. Boris, A. M. Landsberg, E. S. Oran, and J. H. Gardner, LCPFCT - A flux-corrected transport algorithm for solving generalized continuity equations, Technical report No. 93-7192, Naval Research Lab Washington DC, 1993.

[60] J Adams, P Swarztrauber, and R Sweet, Fishpak: A package of fortran subprograms for the solution of separable elliptic partial differential equations, The National Center for Atmospheric Research, Boulder, CO, 1980, http://www.netlib.org/fishpack.

[61] A. Das and P. Kaw, Suppression of Rayleigh Taylor instability in strongly coupled plasmas, Physics of Plasmas **21**, 062102 (2014).

[62] See Supplemental Material at http://link.aps.org/supplemental/10.1103/PhysRevE.102.043216 for a visualization that accompanies the static images shown in Fig. 2.

[63] H. Ikezi, Coulomb solid of small particles in plasmas, Phys. Fluids **29**, 1764 (1986).

[64] M. A. Allessie, F. I. M. Bonke, and F. J. G. Schopman, Circus movement in rabbit atrial muscle as a mechanism of tachycardia. II, Circ Res **39**, 168 (1976).

[65] G. T. Gerisch, Stadienspezifische aggregationsmuster beidictyostelium discoideum, Wilhelm Roux'Archiv fur Entwicklungsmechanik der Organismen **156**, 127 (1965).

[66] E. Bodenschatz, J. R. de Bruyn, G. Ahlers, and D. S. Cannell, Transitions Between Patterns in Thermal Convection, Phys. Rev. Lett. **67**, 3078 (1991).

[67] M. Net, I. Mercader, and E. Knobloch, Binary fluid convection in a rotating cylinder, Phys. Fluids **7**, 1553 (1995).

[68] K. Agladze and O. Steinbock, Waves and vortices of rust on the surface of corroding steel, J. Phys. Chem. A **104**, 9816 (2000).

[69] A. Gupta and R. Ganesh, Compressibility effects on a shear flow in strongly coupled dusty plasma. I. A study using computational fluid dynamics, Physics of Plasmas **25**, 013705 (2018).